Journal of Luminescence 293 (2026) 121844

Contents lists available at ScienceDirect

Journal of Luminescence

journal homepage: www.elsevier.com/locate/jlumin

Full Length Article

# Spectroscopic characterization of bismuth active centres in germanosilicate optical fibers: Impact of Ge concentration on E–S band amplifier gain

Arindam Halder *, Zahra Kakaei **

*Optoelectronics Research Centre, University of Southampton, B53, Highfield Campus, Southampton, SO17 1BJ, United Kingdom*

ARTICLE INFO

*Keywords:*
Bismuth doped optical fiber
Bismuth spectroscopy
E-S band amplifier
Optical fiber material
Optical fiber fabrication

ABSTRACT

A spectroscopic study on bismuth active centres (BACs) with variation of germanium ($GeO_2$) concentration in bismuth doped germanosilicate optical fibers (BGSFs); fabricated by MCVD and solution doping technique; is reported based on absorption and emission spectra to explain E-S band amplifier gain. Three types of BACs are demonstrated i.e. Bi-Si, Bi-Si-Ge and Bi-Ge in BGSFs; having bismuth oxidation state predicted as Bi(0); responsible for the observed absorption, emissions and E-S band gain. BGSF with ~7mol% $GeO_2$ produced 41 dB gain with 4.3 dB noise figure (NF) at 1440 nm in a single pass configuration, appeared as the best. The investigation will be helpful to generate efficient bismuth doped fiber amplifiers (BDFA) applicable for E-S band.

## 1. Introduction

Currently, there is a high demand for fast, high-quality digital data transfer in telecommunications, networking, free-space signaling, deep-sea, and space communications. This demand has grown significantly with the advent of 5G technology. In this context, optical fiber-based cables, amplifiers, and sensors have emerged as preferred options for building advanced networking devices due to their long lifespan, low maintenance, low signal transmission loss, and compact size. As a result, the need for high-quality optical fiber amplifiers operating in telecommunication bands has increased [1]. Well-known fiber amplifiers include erbium-doped fiber amplifiers (EDFAs) for the C and L [2–4]; and bismuth-doped fiber amplifiers (BDFAs) for the O, E, S, and U bands [4–7]. Among these, BDFAs have gained particular attention for their broad operating range (1100-1800 nm), where no alternative rare-earth-doped fiber amplifiers are available [4,6,8].

The operational window of BDFAs can be tailored by selecting appropriate host glasses. For instance, phosphosilicate hosts enable amplification in the O-band and O + E bands, germano-silicate glasses with less than 50 mol% $GeO_2$ support E + S band operation, and hosts with more than 50 mol% $GeO_2$ facilitate U-band amplification [4,7]. Bismuth (Bi) exists in multiple oxidation states within glass hosts, making the development of a comprehensive spectroscopic model to explain amplifier performance particularly challenging [4,7,8]. Gains approaching 40 dB in the O-band and E + S bands have been reported for BDFAs using phosphosilicate and germanosilicate hosts respectively, although device lengths exceeding 50 m were typically required [4,9,10]. More recent studies have demonstrated E + S band BDFAs with device lengths below 50 m [5,10,11], yet a not clear understanding of how to simultaneously achieve high gain and reduced fiber length. It has been suggested that the requirement for long fiber lengths stems from the low Bi concentration in the fibers, posing additional fabrication challenges [4,8,10]. Some reports have explored spectral properties of BDFAs using germanosilicate fibers with varying $GeO_2$ and Bi concentrations under different fabrication conditions [12]. Further studies have also investigated energy state diagrams, local environments, and Bi oxidation states across various glass hosts [8,13–17]. Notably, it has been shown that adjusting the $GeO_2$ content from 5 to 100 mol% enables tuning of BDFA operation across the E, S, and U bands [18]. Nonetheless, a comprehensive understanding of the combined effects of $GeO_2$ and Bi concentration on E + S band BDFA performance remains an open area of research.

In this article, a detailed spectral study on the role of $GeO_2$ in achieving high E + S band gain, specifically, a maximum gain of 40.99 dB with a noise figure (NF) of 4.3 dB at 1440 nm, is presented. Multiple BGSFs with varying $GeO_2$ contents (correlated with the fibers' numerical apertures) and Bi concentrations (related to absorbance at 1400 nm) were investigated, all fabricated using the MCVD process combined with solution doping. A comprehensive spectral analysis was conducted, tracking Bi absorption bands between 370 and 1800 nm and Bi

* Corresponding author.
** Corresponding author.
*E-mail addresses:* arindam.cgcri@gmail.com (A. Halder), zahrakakaie@gmail.com (Z. Kakaei).

https://doi.org/10.1016/j.jlumin.2026.121844
Received 22 September 2025; Accepted 6 March 2026
Available online 7 March 2026

**Table 1**
Fiber samples details.

| Fiber sample | Soot deposition temperature used (°C) | Fiber core, clad diameter measured by IFA-100 | Fiber NA | $GeO_2$ (mol%) in core calculated using [18] |
|---|---|---|---|---|
| BGSF-1 | 1350 | 7.92 μm, 125.80 μm | 0.12 | 3.57% |
| BGSF-2 | 1275 | 6.98 μm, 125.23 μm | 0.16 | 5.36% |
| BGSF-3 | 1275 | 7.08 μm, 99.23 μm | 0.19 | 7.86% |
| BGSF-4 | 1325 | 9.05 μm, 100.00 μm | 0.22 | 10.7% |
| BGSF-5 | 1275 | 7.08 μm; 100.13 μm | 0.26 | 15.71% |
| BGSF-6 | 1275 | 7.08 μm, 99.45 μm | 0.29 | 20.00% |
| BGSF-7 | 1325 | 7.45 μm, 100.66 μm | 0.32 | 22.86% |
| BGSF-8 | 1350 | 6.52 μm, 100.76 μm | 0.18 | 7.45% |
| BGSF-9 | 1325 | 9.31 μm, 102.58 μm | 0.26 | 15.71% |

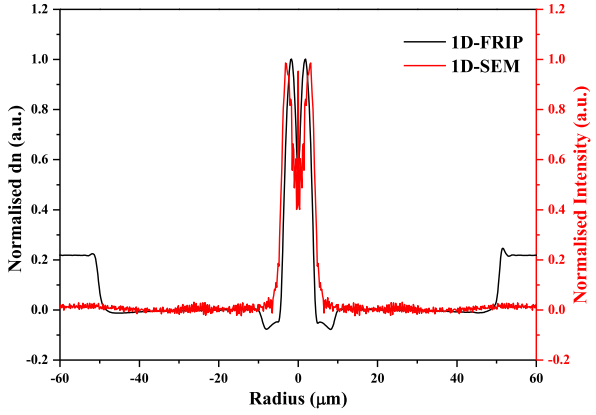


**Fig. 1.** Normalised FRIP and SEM plots for BGSF-3.

emissions under excitations at 450 nm, 792 nm, and 1310 nm. Based on this analysis, a probable explanation for the superior gain performance of BGSFs containing ~7 mol% $GeO_2$ is proposed. These findings provide valuable insights for the future development of high-performance BDFAs targeting the E + S band.

## 2. Experiments

### 2.1. Fabrication of fiber samples

BGSF preforms were fabricated using the conventional modified chemical vapour deposition (MCVD) process in combination with the solution doping (SD) technique. Initially, three $SiO_2$ cladding layers were deposited at 2000 °C inside an F300-grade silica substrate tube of ODxID: 20 × 16 mm (Heraeus Tenvo, Suprasil) loaded on MCVD lathe. Subsequently, a single $SiO_2$-$GeO_2$ soot layer was deposited atop the cladding layers at temperatures ranging from 1275 °C to 1350 °C. By varying the flow ratios of $SiCl_4$ and $GeCl_4$, a range of $GeO_2/SiO_2$ concentrations in the core was achieved. Soot deposition temperatures were optimised to produce high-porosity soot layers, which were found to be strongly dependent on the $GeO_2/SiO_2$ ratio.

Following deposition, the tube was removed from the lathe and soaked for approximately 1 h in Bi solutions of varying concentrations to introduce different bismuth doping levels into the core. After draining the solution, the wet soot layer was dried properly in air for ~1 h, and then on lathe with He-$N_2$ gas mixture for ~1 h. Followed by two oxidation passes using $O_2$ at 1000 °C and 1200 °C were applied to convert $BiCl_3$ to bismuth oxides ($Bi_xO_y$). One sintering pass at 1800 °C in an $O_2$-He atmosphere was performed to consolidate the soot into dense core glass. Finally with collapse and sealing passes at 2175 °C and ~2190 °C, respectively, tube was converted to a solid preform.

Optical fibers with core diameters of 100-125 μm were drawn from these preforms using a silica fiber drawing tower. The drawing was performed at 2000 °C with a draw speed of 10 m/min and a tension of 70-80g. The fibers were coated with a high-index polyacrylate (Desolite, DSM-314). The key fabrication parameters are summarised in Table 1.

Bismuth-doped samples BGSF-1 to BGSF-7 exhibit relatively high Bi concentrations (except BGSF-6), as indicated by the absorption peak near ~1400 nm (Fig. 2a and b). BGSF-8 and BGSF-9 are lower Bi concentration variants of BGSF-3 and BGSF-5, respectively (Fig. 2a and b). Samples BGSF-1 to BGSF-7 were used to investigate the influence of $GeO_2$ concentration on E–S band amplification, while BGSF-3, 5, 8, and 9 were analysed to study the effect of Bi concentration on optimised device lengths.

### 2.2. Bismuth active centres distribution analysis of fiber samples

The fiber refractive index profiles (FRIPs) of the BGSFs were measured using an IFA-100 Interferometric Fiber Analyser using a bare section of each fibers, mounted on the sample chamber of the IFA-100, and measure one-dimensional (1D) FRIP using 1D-FRIP program and white light source. Further, 1D spontaneous emission mapping (SEM) of bismuth active centres (BACs) was performed using the 1D-SEM program under 450 nm side-pumping, detecting 827–940 nm emission (Fig. 3a and b) via a charge-coupled device (CCD), using a 490 nm filter to block pump light, in front of it; at IFA-100. The emission profiles were compared with RIPs using normalisation of both 1D-FRIP and 1D-SEM and overlapping each other (Fig. 1) to locate BACs within the core and assess possible Bi diffusion beyond the active region. Such diffusion may result in non-emissive Bi species that do not participate in the optical processes, highlighting the importance of this characterisation step in evaluating the integrity of the doping process.

### 2.3. Spectroscopic study of fiber samples (absorption, emission, etc.)

Bi absorption spectra and background attenuation spectra of the BGSFs were measured using the cut-back technique. BGSFs were illuminated by a broadband white light using a standard single-mode fibers (SMFs) as a launch fiber. BGSFs were spliced with the launch fiber to couple light directly at BGSFs' cores and transmitted signals were detected using an optical spectrum analyser (OSA; AQ-6315A, Yokogawa) from the other end of BGSFs which further splices with another launch fiber. Splices with losses of ~0.01-0.05 dB were selected to minimise measurement error. All measurements were repeated 3-4 times to ensure repeatability. The fiber lengths were selected targeting to get a well resolve spectra above the noise level of OSA particularly for Bi absorptions. The test results were summarised in Fig. 2 a, b, c, d

Emission spectra were measured under 5-30 mW pump powers at 450 nm, 792 nm, and 1310 nm. BGSF lengths of ~15 cm, 30 cm, and 80 cm were used respectively, increasing with pump wavelength due to reduced BAC absorption. Fiber lengths were kept under 1 m to prevent induced emission generation. The output was monitored using an OSA (AQ-6315A, Yokogawa), either directly or via an SMF splice. Emission spectra under different excitations are shown in Fig. 3

Absorption and emission spectra were analysed to explain the down-conversion process using a schematic energy level diagram of BACs (section 3.4). Emission under various excitation wavelengths helped identify different BAC types across the 350-1800 nm range, as discussed in later sections.

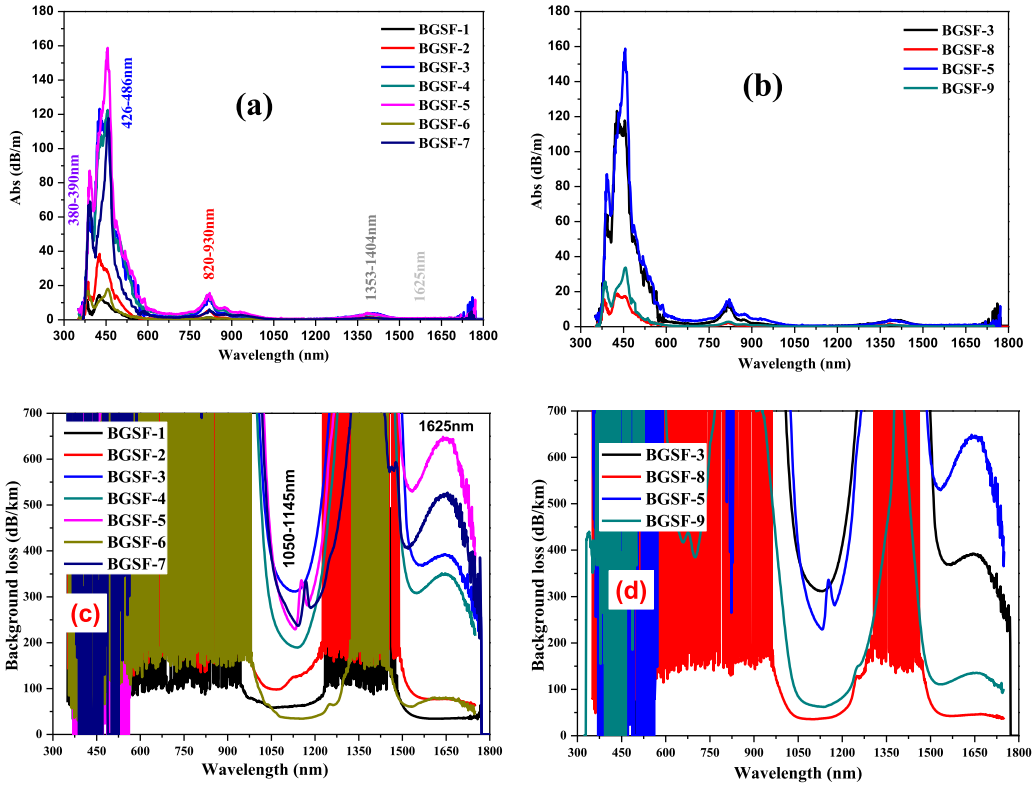


**Fig. 2.** Absorption spectra **(a)** for BGSF-1 to 7, and **(b)** for BGSF-3, 5, 8, 9; Background losses **(c)** for BGSF-1 to 7, and **(d)** for BGSF-3, 5, 8, 9.

### 2.4. E-S band amplification of fiber samples

E–S band gain (G) and noise figure (NF) were measured using a single-pass amplifier setup (Fig. 4), where the BGSFs (FUT) were spliced to wavelength division multiplexing (WDM) pigtails. A tunable laser source (TLS) with a variable attenuator was used to supply input signals of −10 dBm and −23 dBm over 1400-1500 nm. Forward pumping was provided by a 1333 nm laser (440 mW), and counter-pumping by two combined 1310 nm lasers (689 mW). G and NF were computed using standard formulas:

G at wavelength λ:

$$G_\lambda(dB) = 10\,log\frac{P(\lambda)_{out}}{P(\lambda)_{in}} \quad (1)$$

NF at wavelength λ:

$$NF_\lambda\,(dB) = 10\,\log\left(\frac{N(\lambda)_{out} - N(\lambda)_{in}G_\lambda}{h\nu G_\lambda B_0} + \frac{1}{G_\lambda}\right) \quad (2)$$

Here, Pin/out(λ) are the input/output signal peak powers, Nin/out(λ) are the noise powers, h is Planck's constant, $\nu$ is optical frequency, and $B_0 = c/(\lambda R)$ is the OSA resolution bandwidth, where c is the speed of light and. $G_\lambda$ is used in linear units for NF calculations.

The best E-S band G and NF for optimised device lengths of BGSFs are summarised in Table 2. A comparative plot of G and NF for BGSF-1 to 7 (excluding BGSF-6) is shown in Fig. 5. Fig. 6 shows the dependence of **(a)** G and NF, **(b)** unsaturable loss at 1333 nm, and **(c)** optimised device length on $GeO_2$ concentration. BGSF-6 was excluded due to its low Bi content and unoptimised length, due to insufficient stock fiber length. These results are discussed in more detail later.

## 3. Results and discussions

### 3.1. Fabrication and Bi confinement at core glass

The primary fabrication challenges of BGSFs using $GeO_2$–$SiO_2$ soot layers was maintaining soot stability and porosity. Various deposition temperatures were used tally with different $GeCl_4/SiCl_4$ flow ratios (to create Ge concentration difference) to optimise soot porosity for effective Bi incorporation via solution doping (Table 1). Soot porosity, which directly influenced Bi uptake, depended heavily on deposition temperature. Poorly optimised deposition led to issues such as soot detachment, cracking, low Bi levels, and dopant inhomogeneity. Thus, precise control of the fabrication process was essential. Fig. 1 confirms that the BACs responsible for 827 nm and 940 nm emissions (Fig. 3a and b) remained well-confined to the core in BGSF-3, indicating minimal diffusion. The core's refractive index difference (Δn) was primarily determined by the $GeO_2$ concentration [18].

### 3.2. Absorption, base attenuation, and emission spectra

The absorption spectra in Fig. 2a and **(b)** clearly demonstrate that all BGSFs exhibit four main absorption bands with peaks in the ranges of 380–390 nm, 426–486 nm, 820–930 nm, and 1353–1625 nm. Fig. 2a illustrates the shift in Bi absorption peaks with varying $GeO_2$ and Bi concentrations across BGSF-1 to BGSF-7. Fig. 2b presents the changes in absorbance as a function of Bi concentration at fixed $GeO_2$ levels, specifically for BGSF-3, 5, 8, and 9. Notably, BGSF-3 and BGSF-8 contain 7.86 mol% and 7.45 mol% $GeO_2$, respectively, while BGSF-5 and BGSF-9 both have 15.71 mol% $GeO_2$ in their cores.

A noticeable change in peak pattern within 400-600 nm absorption band was observed across samples BGSF-1 to BGSF-7, despite differences in Bi content. For BGSF-1, a single absorption peak appears at 426 nm, which splits into two distinct peaks at 426 nm and 455 nm in BGSF-3. In

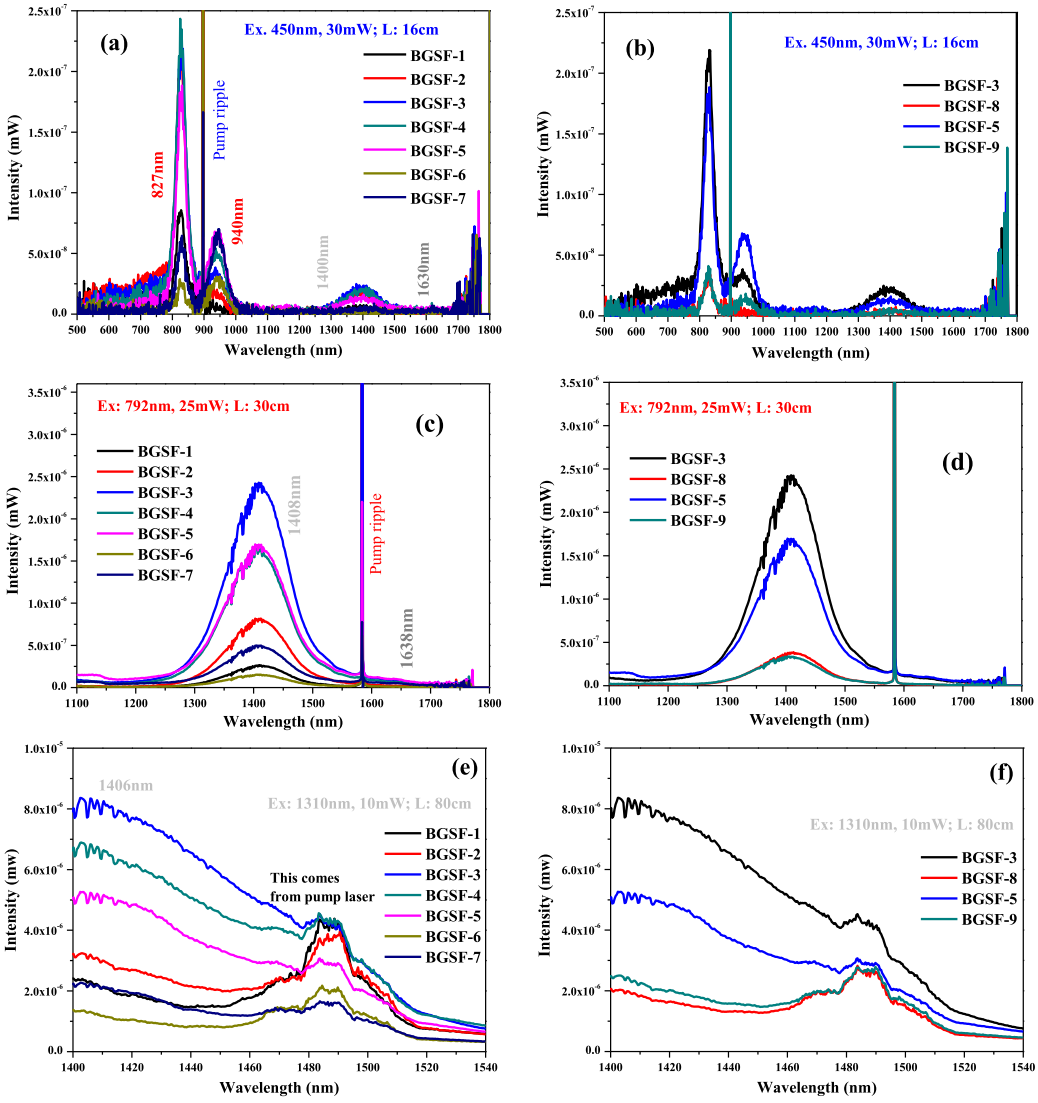


**Fig. 3.** Emission spectra for BGSF-1 to 7 using pump at **(a)** 450 nm, **(c)** 792 nm, and **(e)** 1310 nm; and emission for BGSF-3, 5, 8 and 9 under **(b)** 450 nm, **(d)** 792 nm and **(f)** 1310 nm excitations.

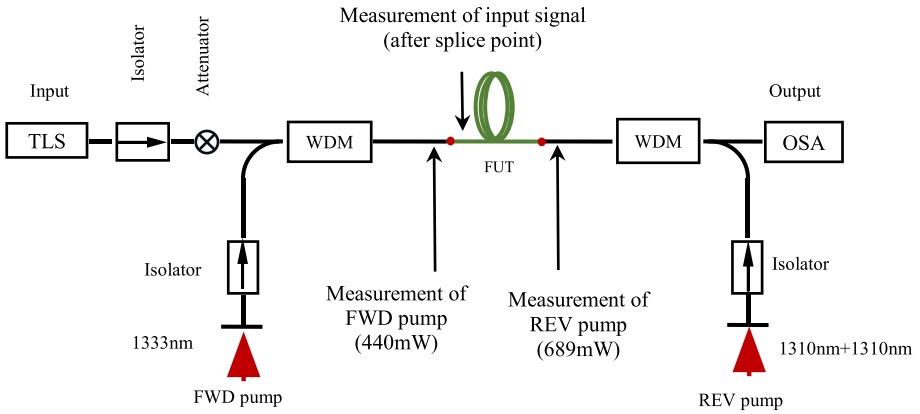


**Fig. 4.** Schematic experimental design of single pass amplifier for E-S band BGSFAs.

BGSF-4 to BGSF-7, the 455 nm peak becomes dominant, shifting slightly to 457 nm. Additionally, a weaker absorption peak around 486 nm is consistently present in all BGSFs, as shown in Fig. 7. To explore the evolution of the 455/457 nm and 486 nm peaks relative to the 426 nm band, all spectra were normalised to the 426 nm peak and plotted together in Fig. 7a. The variation in peak intensities with $GeO_2$

**Table 2**
Amplifier performance and unsaturable loss details.

| Fiber sample | Optimised device length | Maximum G (dB) observed at 14xxnm | | NF (dB) at 14xxnm | | Unsaturable loss at 1333 nm |
|---|---|---|---|---|---|---|
| | | −23dBm input signal | −10dBm input signal | −23dBm input signal | −10dBm input signal | |
| BGSF-1 | 257m | 13.007 @1450 nm | 12.231 @1450 nm | 5.9221 @1450 nm | 6.0864 @1450 nm | 32.5% |
| BGSF-2 | 150m | 38.976 @1440 nm | 29.255 @1440 nm | 3.946 @1440 nm | 3.8349 @1440 nm | 19.1% |
| BGSF-3 | 46m | 40.993 @1440 nm | 31.434 @1440 nm | 4.3481 @1440 nm | 3.9097 @1440 nm | 14.29% |
| BGSF-4 | 55m | 36.845 @1440 nm | 30.005 @1440 nm | 3.9047 @1440 nm | 4.1638 @1440 nm | 12.47% |
| BGSF-5 | 86m | 36.503 @1440 nm | 28.141 @1440 nm | 5.9321 @1440 nm | 5.1519 @1440 nm | 17.28% |
| BGSF-6 | 191m | 7.647 @1450 nm | 6.528 @1450 nm | 5.0518 @1450 nm | 5.8466 @1450 nm | 35.29% |
| BGSF-7 | 96m | 20.748 @1440 nm | 17.961 @1440 nm | 5.4338 @1440 nm | 6.1564 @1440 nm | 22.58% |
| BGSF-8 | 252m | 36.524 @1440 nm | 28.205 @1440 nm | 4.0885 @1440 nm | 4.3347 @1440 nm | 11.06% |
| BGSF-9 | 272m | 27.69 @1440 nm | 23.57 @1440 nm | 7.212 @1440 nm | 6.7633 @1440 nm | 14.70% |

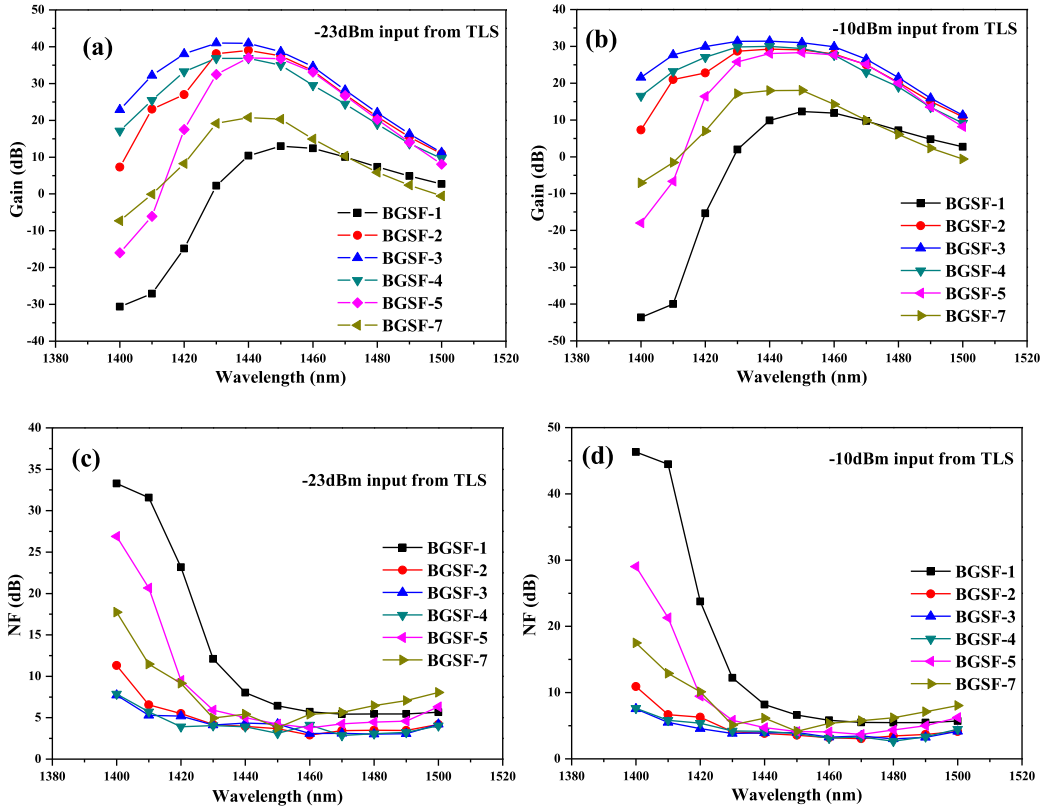


**Fig. 5.** (a), (b) E-S band G and **(c), (d)** NF for BGSFs 1-7 (except BGSF-6).

concentration is shown in Fig. 7b. The results indicate that the 455/457 nm peak increases gradually with rising $GeO_2$ content, becoming more prominent than the 426 nm peak from BGSF-3 onward (which contains ~7 mol% $GeO_2$). In BGSF-3, both peaks are of comparable intensity. The 486 nm band also intensifies gradually with increasing $GeO_2$ concentration. To qualitatively assess overlapping absorption features, Gaussian multi-peak fitting was performed using OriginLab. Fig. 7c shows the fitted peaks for BGSF-3, highlighting the presence of absorption bands at 393 nm, 426 nm, 455 nm, and 486 nm.

In the 700-1050 nm absorption region, three-band overlapping structure is also observed, similar to the pattern seen in the 400–600 nm range. To analyse this, the spectra were normalised to the 820 nm peak, and the evolution of the 875 nm and 930 nm peaks was examined with respect to the 820 nm peak and $GeO_2$ concentration (Fig. 8a and b). The results clearly show that both the 875 nm and 930 nm peaks gradually intensify with increasing $GeO_2$ content in the core glass of the BGSFs. Fig. 8c presents the Gaussian multi-peak fitting for BGSF-3, confirming the presence of these three absorption bands.

Three overlapping absorption bands are also expected within the 1100–1800 nm range. Among them, two distinct bands at 1385 nm and 1625 nm were clearly observed in the absorption and base attenuation spectra (Fig. 2). To investigate further, the spectra of BGSF-1 to 7 were normalised at 1385 nm and presented in Fig. 9a. The variation of the 1625 nm peak relative to 1385 nm, with increasing $GeO_2$ concentration, is shown in Fig. 9b. Using Gaussian multi-peak fitting, three absorption bands within this range were identified for BGSF-3 and are shown in Fig. 9c. Note: the 1353 nm band consistently merges with the 1404 nm band in the true absorption spectra (see Figs. 2 and 9c), making it difficult to track their individual evolution in the normalised plot (Fig. 9a). Therefore, the 1353 nm band was excluded from Fig. 9b.

An increase in the prominence of the 1625 nm peak with higher $GeO_2$ concentration in the core is also evident in the base attenuation spectra (Fig. 2c) for fibers BGSF-1 to 7. This trend indicates that the 1625 nm feature becomes progressively more pronounced with increasing $GeO_2$ content in the core glass.

In the emission spectra shown in Fig. 3a, three main emission bands

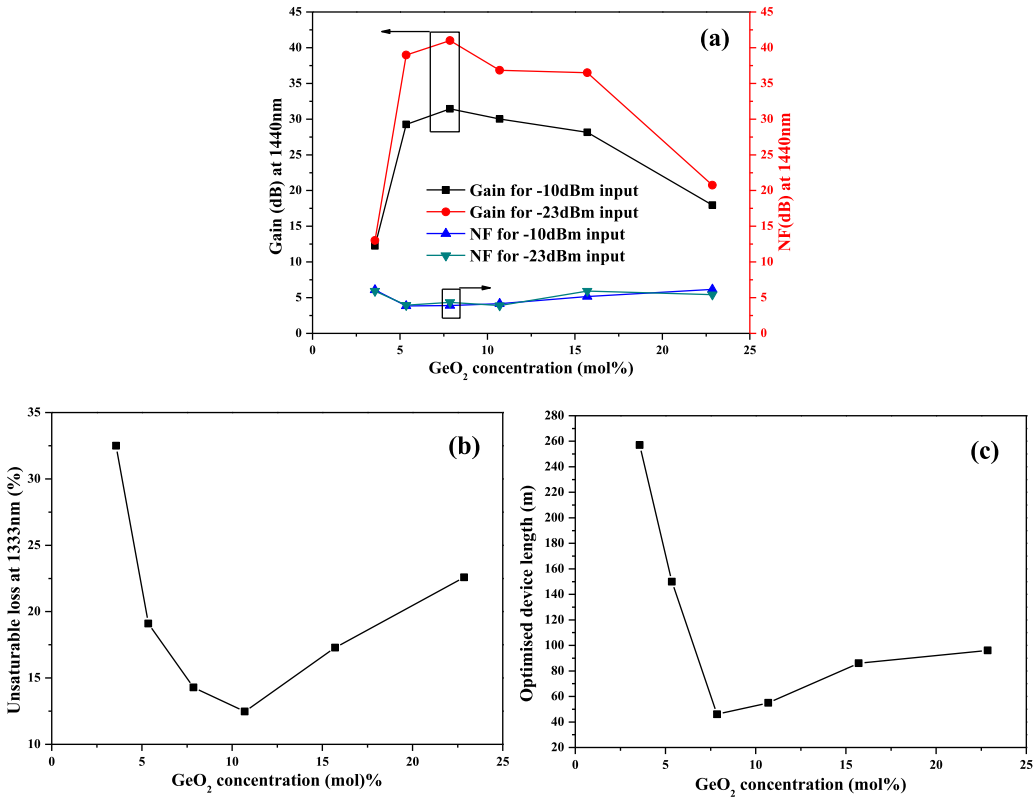


**Fig. 6.** (a) variation of E-S band G and NF; **(b)** unsaturable loss and **(c)** optimised device length with $GeO_2$ concentration of the BGSFs (1 to 7, except 6).

at 827 nm, 940 nm, and 1400 nm are observed under 450 nm laser excitation. A very weak emission around 1630 nm is also detected for BGSF-6 and BGSF-7 under the same excitation. Under 792 nm excitation, only the 1408 nm emission band appears prominently (Fig. 3c), along with a weak 1638 nm emission primarily in BGSF-6 and BGSF-7. For in-band excitation at 1310 nm, only a 1406 nm emission band is observed, partially overlapped by the spectral tail of the laser source (Fig. 3e). A similar emission pattern is seen for the low Bi-content fibers, BGSF-8 and BGSF-9, which have approximately 7 mol% and 15 mol% $GeO_2$ in the core, respectively. Notably, BGSF-3 and BGSF-5, which have higher Bi content, exhibit comparable emission characteristics (Fig. 3b, d, 3f). These findings suggest that the nature of the BACs is consistent across all fibers. However, these emission results alone cannot fully explain the unsaturable loss (UL) patterns observed in Fig. 6b, indicating the need for a more detailed understanding of BAC behavior, as discussed in Section 3.4.

Under 450 nm excitation, a notable change is observed in the relative emission intensities of the 827 nm and 940 nm bands. The low $GeO_2$-content fibers, such as BGSF-1 and BGSF-2, exhibit strong emission at 827 nm and very weak emission at 940 nm. As the $GeO_2$ concentration increases, the intensity of the 940 nm band gradually rises, while the 827 nm band shows a slight reduction in intensity. The 940 nm emission reaches its maximum for fibers BGSF-6 and BGSF-7, which have the highest $GeO_2$ content. To illustrate this trend, the 827 nm peak was used for normalisation, and the relative intensity of the 940 nm peak with increasing $GeO_2$ concentration is plotted in Fig. 10a and b. These figures also show the variations of the 1400 nm and 1630 nm emission bands. From Fig. 10b, it is evident that the 1400 nm emission reaches its maximum intensity in BGSF-3, after which it gradually diminishes. The weak 1630 nm band surpasses the 1400 nm band in intensity for BGSF-6 and becomes more dominant in BGSF-7.

For emission under 792 nm excitation, the 1408 nm peak was used for normalisation across all BGSFs, and the results are presented in Fig. 10c. The variation of the weak 1638 nm band relative to the 1408 nm peak is shown in Fig. 10d. It is observed that the 1638 nm emission gradually intensifies with increasing $GeO_2$ concentration in the core, from BGSF-1 to BGSF-7. A detailed explanation of these spectral observations, supported by a schematic energy level diagram of the BACs derived from the absorption and emission behavior of the BGSFs, is provided in Section 3.4.

### 3.3. E-S band amplifier

From Figs. 5 and 6a, and Tables 2 and it is observed that BGSF-3, with ~7 mol% $GeO_2$ in the core (Table 1), exhibits the highest G of 40.933 dB and the lowest NF of 4.3481 dB at 1440 nm, under a −23 dBm input signal from the TLS, compared to all other BGSFs. Additionally, Figs. 5 and 6a show that the G decreases both below and above the ~7 mol% $GeO_2$ concentration. However, fibers BGSF-2, BGSF-4, and BGSF-5 also demonstrate comparable G, with only a ~2-3 dB difference relative to BGSF-3. This G pattern may be influenced by the nature of the BACs generated within the BGSFs. To understand this relationship more clearly, a deeper investigation into the BACs configuration is necessary, as discussed in Section 3.4.

From the UL data in Fig. 6b, it is evident that BGSF-4 has the lowest UL, while BGSF-3 shows a slightly higher value. Again, understanding this trend requires a thorough analysis of the BACs, which is also addressed in Section 3.4. Moreover, Fig. 6b and Table 2 reveal that UL remains below 20% for fibers BGSF-2 to BGSF-6. Among these, BGSF-2 to BGSF-5 each achieve G above 30 dB. Therefore, it can be concluded that BGSFs with less than 20% UL under 1333 nm pumping and a $GeO_2$ concentration ranging 5-15 mol% (Table 1) are capable of producing G near or above 30 dB in the E-S band for a −23 dBm input signal. Hence, UL may serve as a secondary factor influencing the G output observed in the BGSFs discussed here.

In this context, the G values of BGSF-8 (~7 mol% $GeO_2$) and BGSF-9

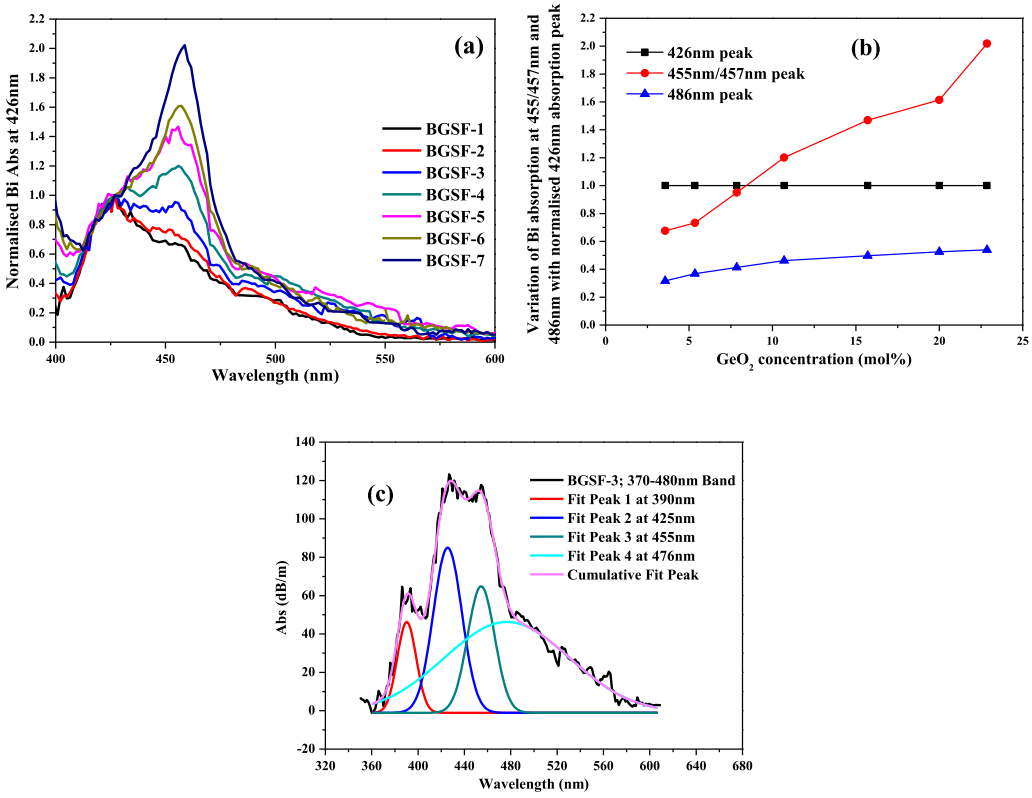


**Fig. 7.** (a) Normalised 400-600 nm absorption band; **(b)** variation of 455nm/457 nm and 486 nm absorption peak along with 426 nm peak in BGSFs (BGSF-1 to 7) with $GeO_2$ concentration obtained from Fig. 7a; **(c)** Gaussian multipeak fitting for BGSF-3 in 350-600 nm to track 390 nm, 426 nm, 455 nm and 486 nm absorption bands from true absorption spectra.

(~15 mol% $GeO_2$), both with lower Bi concentrations than BGSF-3 and BGSF-5 respectively, show a noticeable drop, consistent with their lower absorption at 1385 nm (Fig. 2). BGSF-8 exhibits higher G than BGSF-9, reflecting the trend seen between BGSF-3 and BGSF-4. The lower Bi content likely accounts for the reduced G and the longer device lengths required for BGSF-8 and BGSF-9 (Table 2), compared to BGSF-3 and BGSF-5.

Despite this, the device length and UL patterns for BGSF-8 and 9 still align with the trends observed in BGSF-3 and 5 as a function of $GeO_2$ concentration (Fig. 6b and c). When analysing the influence of Bi concentration (Fig. 11), a clear trend emerges only when $GeO_2$ is fixed (Fig. 11b). When both Bi and $GeO_2$ vary (Fig. 11a), no consistent pattern is seen. This suggests device length is primarily governed by $GeO_2$ content, while Bi concentration plays a secondary role when $GeO_2$ is held constant. A more detailed investigation with controlled samples is needed to confirm this, which could be addressed in future work to avoid extending the current manuscript.

### 3.4. Discussion on spectral observations

All BGSFs exhibit ground-state absorption bands at 380–390 nm, 426-486 nm, 820-930 nm, and 1400-1625 nm (Fig. 2), with corresponding emissions at 827-940 nm and 1400-1640 nm regions (Fig. 3). No additional absorption features were detected in any samples, indicating that the nature of BACs is consistent across all BGSFs. Literature reports [8,17] suggest that Bi in the zero-oxidation state, Bi(0), is responsible for similar absorption and emission characteristics. Within each absorption region, three overlapping bands [12,19] are observed (Figs. 7–9), attributed to chemical shifts in Bi absorption caused by variations in the local environment. The host glass used is a germano-silicate with $GeO_2$ concentrations ranging from 3.57 to 22.86 mol% (Table 1), likely giving rise to three distinct Bi environments: (i) Si-rich, (ii) Si-Ge mixed, and (iii) Ge-rich. Consequently, three types of BACs are observed: Bi-Si, Bi-Si-Ge, and Bi-Ge [13], which manifest as the overlapping absorption bands in Figs. 7–9. A schematic energy level diagram (Fig. 12), based on experimental observations and literatures [8,12,13,17,19], are proposed for the Bi spectral processes. Assumed that all BGSFs contain over 75 mol% $SiO_2$, and both $SiO_4$ and $GeO_4$ form similar structural units, Bi may preferentially occupy Si sites. This would result in a higher concentration of Bi-Si centres relative to Bi-Si-Ge and Bi–Ge, as shown in Fig. 12. Comparing Figs. 7–9 with Fig. 12 also reveals that the absorption features linked to Bi-Si-Ge and Bi-Ge centres intensify with increasing $GeO_2$ content in the core glass.

In the absorption spectra (Fig. 2a and b), the strongest peak appears at 426-486 nm, corresponding to the $^4S_{3/2} \rightarrow {}^2P_{1/2}$ transition. This is followed by a weaker absorption band at 820-930 nm ($^4S_{3/2} \rightarrow {}^2D_{5/2}$), and the weakest absorption occurs at 1353-1625 nm ($^4S_{3/2} \rightarrow {}^2D_{3/2}$). The strength of these transitions is governed by three main selection rules: (i) spin angular momentum ($\Delta S = \pm 0$), (ii) orbital angular momentum ($\Delta L = \pm 1$), and (iii) total angular momentum ($\Delta J = \pm 1$). In addition, a symmetry-based selection rule applies, depending on the local point group symmetry around the active Bi atom [20–23].

Among these, the spin selection rule ($\Delta S = \pm 0$) has the highest priority. However, all observed transitions for Bi(0) violate this rule, rendering them spin-forbidden and inherently weak. This explains why a high Bi concentration is required to achieve appreciable absorption in optical fibers. The next most significant rule is $\Delta L = \pm 1$. The 426-486 nm transition involves an S→P transition ($\Delta L = +1$), whereas transitions to D states (820-1625 nm) involve $\Delta L = +2$, which is less favoured. As a result, the 380–486 nm absorption band is stronger than the longer-wavelength bands. Finally, considering the $\Delta J = \pm 1$ rule: the 380-390 nm band involves $\Delta J = 0$; the 426-486 nm band, $\Delta J = -1$; the

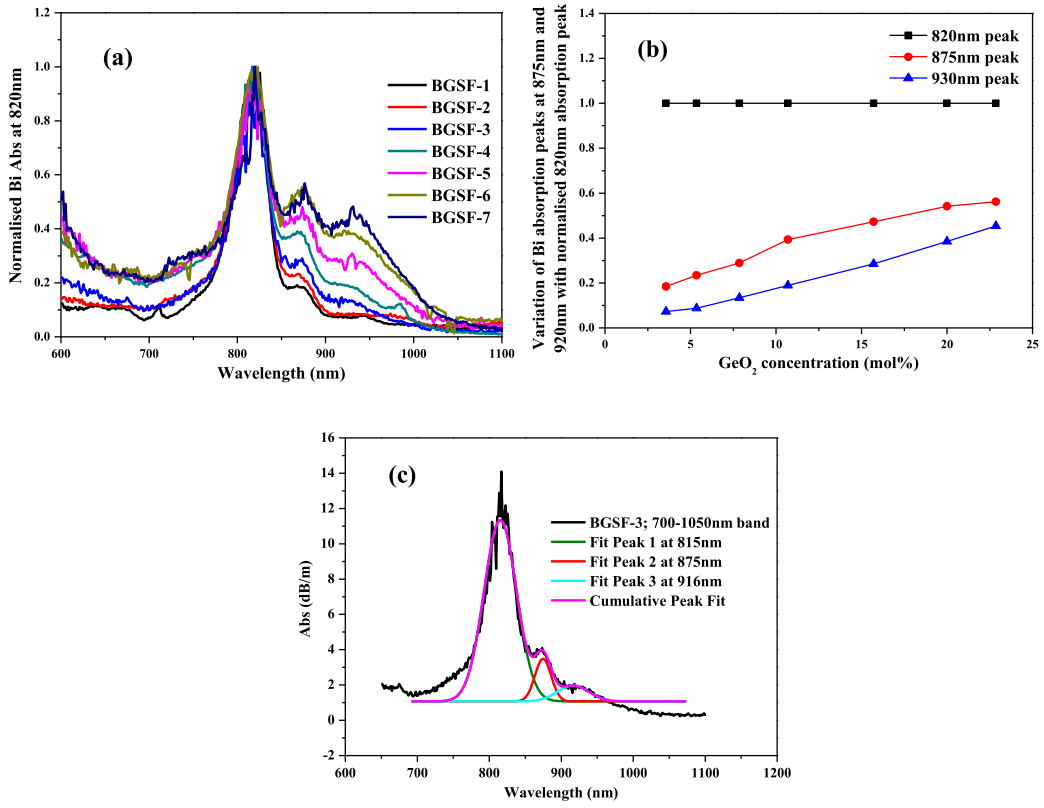


**Fig. 8.** (a) Normalised 700-1050 nm absorption band; **(b)** variation of 875 nm and 930 nm absorption peak along with 820 nm peak in BGSFs (BGSF-1 to 7) with $GeO_2$ concentration obtained from Fig. 8a; **(c)** Gaussian multipeak fitting for BGSF-3 in 700-1050 nm to track 820 nm, 875 nm, 930 nm absorption bands from true absorption spectra.

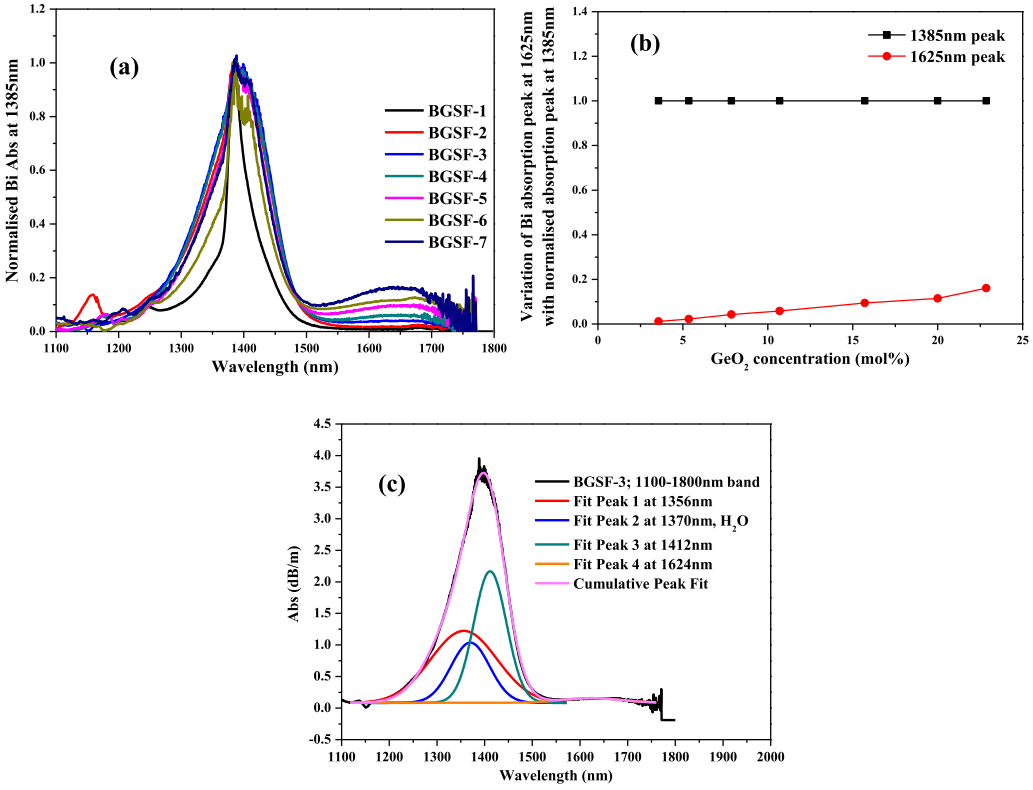


**Fig. 9.** (a) Normalised 1100-1800 nm absorption band; **(b)** variation of 1625 nm absorption peak along with 1385 nm peak in BGSFs (BGSF-1 to 7) with $GeO_2$ concentration obtained from Fig. 9a; **(c)** Gaussian multipeak fitting for BGSF-3 in 1100-1800 nm to track 1353 nm, 1404 nm, 1625 nm absorption bands from true absorption spectra.

820–930 nm band, $\Delta J = +1$; and the 1353-1625 nm band again violates $\Delta J = 0$. Therefore, the strongest absorption appears at 426-486 nm, followed by 380-390 nm and 820-930 nm. The weakest absorption at 1353-1625 nm violates all major selection rules and is governed primarily by the local symmetry environment of Bi(0). A detailed structural analysis would be required to further understand these effects, which is beyond the scope of this study.

All spectral selection rules also apply to the down-conversion emission transitions observed in the emission spectra. No direct emissions from the $^2P_{1/2} \rightarrow {}^4S_{3/2}$ and $^2D_{5/2} \rightarrow {}^4S_{3/2}$ transitions are detected, as they violate the $\Delta S = \pm 0$ rule. However, some spin-allowed transitions are possible from the $^2P_{1/2}$ and $^2D_{5/2}$ levels, as detailed below. Emission via the $^2D_{3/2} \rightarrow {}^4S_{3/2}$ transition occurs through a symmetry-controlled path.

Under 450 nm excitation, Bi(0) is promoted from the ground state $^4S_{3/2}$ to $^2P_{1/2}$. From there, the strongest emission occurs via the $^2P_{1/2}$ to $^2D_{5/2}$ transition, spanning 830-1018 nm, which satisfies both the $\Delta S = \pm 0$ and $\Delta L = +1$ rules (here, the $\Delta J$ rule is not a limiting factor, as the first two are fully valid). A second emission path, $^2D_{5/2}$ to $^2D_{3/2}$, occurs in the 1896-2376 nm range, satisfying $\Delta S = \pm 0$ and $\Delta J = -1$, but it is $\Delta L$ forbidden due to the violation of the orbital angular momentum rule. As a result, this transition is expected to exhibit lower intensity compared to the first. Due to detector limitations, emission in the 1896-2376 nm range could not be measured in this study. The final observed transition, $^2D_{3/2}$ to $^4S_{3/2}$, occurs between 1353 and 1625 nm. This transition violates all three primary selection rules and is governed entirely by symmetry-controlled mechanisms, making it the weakest of all observed emissions.

Under 792 nm excitation, two down-conversion pathways are possible: $^2D_{5/2}$ to $^2D_{3/2}$ (1896-2376 nm) and $^2D_{3/2}$ to $^4S_{3/2}$ (1353-1625 nm). Based on the earlier discussion, the former is expected to produce stronger emission than the latter obeying spin allowed rule. It is also noted that due to energy level splitting influenced by the local environment, actual emission wavelengths may deviate from those proposed in Fig. 12 under practical conditions.

The influence of the surrounding chemical environment on Bi(0) is clearly reflected in the emission spectra, as previously discussed for the absorption spectra. In the case of the 830–1018 nm emission band, two prominent peaks are observed at 827 nm and 940 nm (Fig. 3a and b; 10a, b). These peaks are attributed to site crossover transitions: $^2P_{1/2}$(Bi-Si) $\rightarrow {}^2D_{5/2}$(Bi-Si-Ge) at 830 nm and $^2P_{1/2}$(Bi-Si-Ge) $\rightarrow {}^2D_{5/2}$(Bi-Ge) at 897 nm. These transitions are feasible because Bi remains in its zero-oxidation state across all sites, and the overlapping regions of these environments allow such crossovers. Furthermore, such transitions allow Bi to bypass symmetry-controlled selection rules, as changes in the local point group symmetry enable relaxation of transition constraints. Symmetry point groups impose specific restrictions on optical transition freedoms [20–23].

It is reasonable to assume, by analogy with rare-earth ions [13,24], that Bi may reside in either octahedral or tetrahedral coordination environments within the silica glass network. Bi-Si and Bi-Ge sites typically possess an inversion centre ('i') due to the presence of identical atoms surrounding Bi, whereas Bi-Si-Ge sites lack such symmetry. As a result, Bi-Si and Bi-Ge environments exhibit higher symmetry order, while Bi-Si-Ge sites possess lower symmetry order. The absence of 'i' in Bi-Si-Ge centres enhances their optical activity, making transitions involving these sites more intense. This is clearly observed in the absorption spectra (Fig. 9), where the 1385 nm band, associated with Bi-Si-Ge centres, is stronger than the 1353 nm and 1625 nm bands, which arise purely from symmetry-controlled transitions. A similar trend is also evident in the emission spectra for the $^2D_{3/2}$ to $^4S_{3/2}$ transition (Figs. 3 and 10).

It is also important to note that the relative concentrations of the

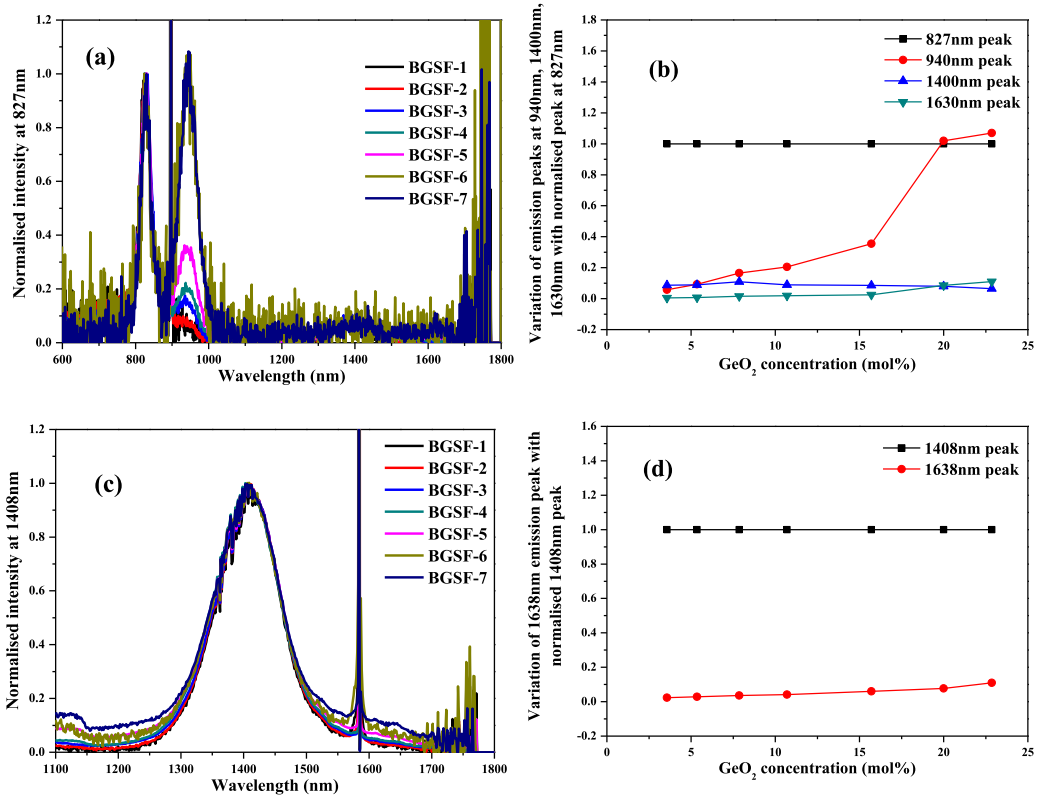


**Fig. 10.** (a) Normalised emission spectra for BGSF-1 to 7 under 450 nm excitation, **(b)** variation of 827 nm, 940 nm, 1400 nm and 1630 nm emissions with $GeO_2$ concentration obtained from Fig. 10a and **(c)** normalised emission spectra for BGSF-1 to 7 under 792 nm excitation, **(b)** variation of 1408 nm and 1638 nm emissions with $GeO_2$ concentration obtained from Fig. 10c.

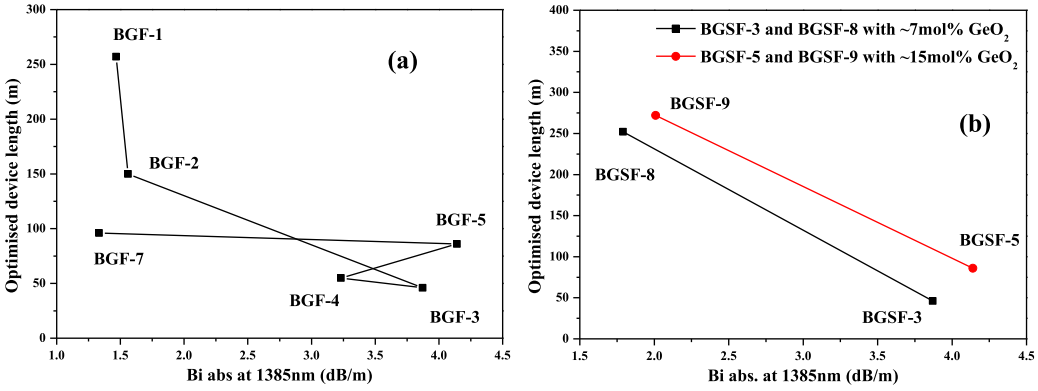


**Fig. 11.** (a) Variation of device length with Bi concentration in different $GeO_2$ content fibers, **(b)** variation of device length with Bi concentration for fixed $GeO_2$ content fibers.

three sites (Bi-Si, Bi-Si-Ge, and Bi-Ge) significantly influence the absorption and emission signal strengths. Sites with higher concentrations naturally contribute more strongly to the spectra. In BGSFs, Bi-Si centres are the most abundant, followed by Bi-Si-Ge and then Bi-Ge, which is present in the lowest concentration. These effects are evident in the absorption comparison plots in Figs. 7 and 8, covering the 380-390 nm, 426-486 nm, and 820-930 nm regions, where primary selection rules are applicable and symmetry-controlled mechanisms play a secondary role.

Energetically, Bi-Si and Bi-Ge sites are more stable than Bi-Si-Ge sites due to their higher order symmetry. Consequently, these higher order symmetry sites require greater activation energy for excitation, leading to weaker emission intensities compared to the lower order symmetry Bi-Si-Ge sites. This explains why BGSF-1, which contains only 5 mol% $GeO_2$, exhibits lower gain at 1440 nm; as it contains fewer Bi-Si-Ge centres. With the $GeO_2$ concentration in the core increases, the number of Bi-Si-Ge centres also increases, resulting in enhanced gain. The gain reaches its maximum in BGSF-3 with 7 mol% $GeO_2$, where Bi-Si and Bi-Si-Ge centres contribute comparably, and a minor contribution from Bi–Ge centres is also present. Beyond BGSF-3, further increases in $GeO_2$ lead to a gain reduction. In fibers BGSF-4 to BGSF-7, Bi-Ge centres dominate the absorption and emission processes. In these higher-$GeO_2$ fibers, a portion of the excited-state population in the $^2D_{3/2}$ level decays via emission around 1630-1638 nm, which competes with and reduces the gain at 1440 nm (Figs. 5 and 6).

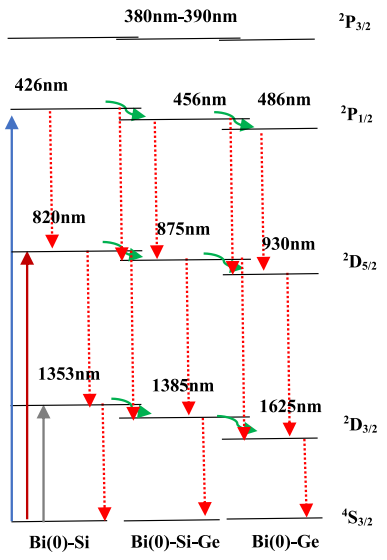


Absorption transitions:

$^4S_{3/2} \rightarrow {}^2P_{3/2}$ : 380-390nm

$^4S_{3/2} \rightarrow {}^2P_{1/2}$ : 426-486nm

$^4S_{3/2} \rightarrow {}^2D_{5/2}$ : 820-930nm

$^4S_{3/2} \rightarrow {}^2D_{3/2}$ : 1353-1625nm

Proposed emission transitions calculated from energy differences between involved energy states:

$^2P_{1/2}$(Bi-Si)$\rightarrow{}^2D_{5/2}$(Bi-Si) : 886nm

$^2P_{1/2}$(Bi-Si-Ge)$\rightarrow{}^2D_{5/2}$(Bi-Si-Ge) : 952nm

$^2P_{1/2}$(Bi-Ge)$\rightarrow{}^2D_{5/2}$(Bi-Ge) : 1018nm

$^2P_{1/2}$(Bi-Si)$\rightarrow{}^2D_{5/2}$(Bi-Si-Ge) : 830nm

$^2P_{1/2}$(Bi-Si-Ge)$\rightarrow{}^2D_{5/2}$(Bi-Ge) : 897nm

$^2D_{5/2}$(Bi-Si)$\rightarrow{}^2D_{3/2}$(B-Si) : 2081nm

$^2D_{5/2}$(Bi-Si-Ge)$\rightarrow{}^2D_{3/2}$(B-Si-Ge) : 2376nm

$^2D_{5/2}$(Bi-Ge)$\rightarrow{}^2D_{3/2}$(B-Ge) : 2174nm

$^2D_{5/2}$(Bi-Si)$\rightarrow{}^2D_{3/2}$(Bi-Si-Ge) : 2010nm

$^2D_{5/2}$(Bi-Si-Ge)$\rightarrow{}^2D_{3/2}$(Bi-Ge) : 1896nm

$^2D_{3/2}$(Bi-Si)$\rightarrow{}^4S_{3/2}$(Bi-Si/Bi-Si-Ge) : 1356nm

$^2D_{3/2}$(Bi-Si-Ge)$\rightarrow{}^4S_{3/2}$(Bi-Si-Ge/Bi-Ge) : 1385nm

$^2D_{3/2}$(Bi-Ge)$\rightarrow{}^4S_{3/2}$(Bi-Ge) : 1630nm

$^2D_{3/2}$(Bi-Ge)$\rightarrow{}^4S_{3/2}$(Bi-Ge) : 1625nm

**Fig. 12.** Schematic energy level diagram of Bi(0) in three chemical environments showing pump excitation (coloured solid upward arrows) and emission (radiative as red downward dotted arrows and non-radiative as green curve arrows). Absorptions and emission transitions are listed in right side boxes. (For interpretation of the references to colour in this figure legend, the reader is referred to the Web version of this article.)

A similar explanation can be applied to the observed UL. The effective absorption of BACs under 1333 nm excitation increases with the abundance of Bi-Si-Ge centres, which have strong absorption near the pump wavelength. However, as the number of Bi-Ge centres increases, the effective absorption decreases because Bi-Ge centres absorb less efficiently at this wavelength. As a result, UL decreases from BGSF-1 to BGSF-3, then increases from BGSF-3 to BGSF-7. This trend is also reflected in the optimal device length (Fig. 6): as effective absorption from Bi-Si-Ge centres increases, the required device length decreases; conversely, when this absorption diminishes, the optimal length increases for amplification at 1310-1330 nm.

In summary, the nature and distribution of BACs are the primary factors determining gain performance and device length, while UL serves as a secondary indicator. Nevertheless, UL remains useful for preselecting suitable fiber samples for amplifier testing. Based on our findings, fibers exhibiting less than 20% UL are most effective for achieving high gain in BGSFs.

## 4. Conclusion

BGSFs were fabricated with an optimised fabrication process using MCVD along with solution doping. E-S band gain, device length, UL variation study is reported using $GeO_2$ concentration variation from 3.57 to 22.86 mol%. 41 dB at 1440 nm gain with 46m device length is appeared as the best from BGSF-3 fiber having 7.86 mol% $GeO_2$ at core.

A complete spectral study using absorption and down-conversion emission under 450 nm, 792 nm and 1330 nm excitation is reported. Under 450 nm pumping strong emission at 827 nm and 940 nm were observed which can further consider for lasing application. Bi oxidation state in BACs is appeared as Bi(0) based on observed absorption and emission spectral pattern as well as in comparison with some literatures [8,17]. Three types of BACs i.e. Bi-Si, Bi-Si-Ge and Bi-Ge were observed depending on the surrounding glass atmosphere of Bi atoms and similar observation is also reported in literature [13]. BGSF-3, with 7.86 mol% $GeO_2$, is appeared as the best over all other fibers in terms of 827 nm emission, E-S band gain etc. This study will be helpful to develop a good E-S band amplifier device, Bi doped fiber lasers in NIR etc. in future.

## Funding

Postdoctoral Fellowship provided by University of Southampton.

## CRediT authorship contribution statement

**Arindam Halder:** Conceptualization, Data curation, Formal analysis, Investigation, Methodology, Project administration, Writing – original draft, Writing – review & editing. **Zahra Kakaei:** Data curation, Formal analysis, Investigation, Writing – review & editing.

## Declaration of competing interest

The authors declare that they have no known competing financial

interests or personal relationships that could have appeared to influence the work reported in this paper.

## Acknowledgement

The authors are thankful to Prof Jayanta Kumar Sahu and staff members of Optoelectronics Research Centre, University of Southampton to provide their postdoctoral fellowships, opportunity for performing research on E-S band bismuth doped fiber amplifier.

## Data availability

All data underlying the results presented in this paper are available in Dataset: https://doi.org/10.5258/SOTON/D3635.

## References

[1] P.J. Winzer, D.T. Neilson, A.R. Chraplyvy, Fiber-optic transmission and networking: the previous 20 and the next 20 years [Invited], Opt. Express 26 (18) (2018) 24190–24239, https://doi.org/10.1364/OE.26.024190.
[2] Z. Zhai, A. Halder, J.K. Sahu, Flat-gain L-band amplifier containing AlPO4 units in aluminophosphosilicate erbium-doped fibers, Opt. Lett. 48 (21) (2023) 5579–5582, https://doi.org/10.1364/OL.503833.
[3] Z. Zhai, A. Halder, D. Negut, J.K. Sahu, Radiation-resistant cerium co-doped erbium-doped fibers for C- and L-band amplifiers in a high-dose gamma-radiation environment, Opt. Express 31 (23) (2023) 38910–38920, https://doi.org/10.1364/OE.502917.
[4] Y. Wang, S. Wang, A. Halder, J. Sahu, Bi-doped optical fibers and fiber amplifiers, Opt. Mater. X 17 (2023) 100219, https://doi.org/10.1016/j.omx.2022.100219.
[5] S. Wang, Z. Zhai, A. Halder, J.K. Sahu, Bi-doped fiber amplifiers in the E+S band with a high gain per unit length, Opt. Lett. 48 (21) (2023) 5635–5638, https://doi.org/10.1364/OL.503912.
[6] A. Vakhrushev, A. Khegai, S. Alyshev, K. Riumkin, A. Kharakhordin, E. Firstova, A. Umnikov, A. Lobanov, F. Afanasiev, A. Guryanov, M. Melkumov, S. Firstov, Cladding pumped bismuth-doped fiber amplifiers operating in O-, E-, and S-telecom bands, Opt. Lett. 48 (6) (2023) 1339–1342, https://doi.org/10.1364/OL.482873.
[7] S. Alyshev, A. Khegai, A. Umnikov, S. Firstov, Bismuth-Doped fiber lasers and amplifiers operating from O- to U-Band: current state of the art and outlook, Photonics 11 (2024) 663, https://doi.org/10.3390/photonics11070663.
[8] A. Halder, A. Kir'yanov, E.H. Sekia, K. Saito, Fabrication and characterization of bismuth-doped germano-silicate and phospho-silicate fibers for VIS/NIR applications, Opt. Mater. Express 9 (4) (2019) 1815–1825, https://doi.org/10.1364/OME.9.001815.
[9] A. Donodin, E. Manuylovich, V. Dvoyrin, M. Melkumov, V. Mashinsky, S. Turitsyn, E-band telecom-compatible 40 dB gain high-power bismuth doped fiber amplifier with record power conversion efficiency, APL Photonics 9 (2024) 046102, https://doi.org/10.1063/5.0187069.
[10] S. Liu, X. Yin, Z. Gu, L. He, W. Li, Y. Chen, Y. Xing, Y. Chu, N. Dai, J. Li, High bismuth-doped germanosilicate fiber for efficient E+ S-band amplification, Opt. Lett. 49 (2) (2024) 314–317, https://doi.org/10.1364/OL.506036.
[11] S. Liu, X. Yin, L. He, Z. Gu, W. Li, Y. Chen, Y. Xing, Y. Chu, N. Dai, J. Li, A 16 m high Bismuth-Doped fiber amplifier provides 47.9 dB gain in E+S-band, in: OFC 2024 Conference, 2024. W1D.2.
[12] V. Fuertes, F.E. Durak, V.A.G. Rivera, N. Grégoire, S. Morency, M. Sharma, L. Wang, Y. Messaddeq, S. LaRochelle, Tailoring optical properties of bismuth-doped germanosilicate fibers for E/S band amplification, J. Non-Cryst. Solids 613 (2023) 122381, https://doi.org/10.1016/j.jnoncrysol.2023.122381.
[13] F. E, D. Zhang, R. Ye, Y. Hua, S. Xu, F. Huang, Structural engineering of germanosilicate glass network for enhanced Bi: NIR luminescence, Opt. Mat. 95 (2019) 109222, https://doi.org/10.1016/j.optmat.2019.109222.
[14] W. Wang, C. Jiang, Anomalous photoemission in bismuth-doped amorphous solid via selective reduction and energy transfer mechanism investigation, J. Alloys Compd. 820 (2020) 153169, https://doi.org/10.1016/j.jallcom.2019.153169.
[15] S.V. Firstov, V.F. Khopin, V.V. Velmiskin, E.G. Firstova, I.A. Bufetov, A. N. Guryanov, E.M. Dianov, Anti-stokes luminescence in Bismuth-doped silica and germania-based fibers, Opt. Express 21 (15) (2013) 18408–18413, https://doi.org/10.1364/OE.21.018408.
[16] A. Mehaboob, V. Fuertes, V.A.G. Rivera, Y. Messaddeq, Tailoring ultrabroadband near-infrared luminescence in Bi-doped germanosilicate glasses, Sci. Rep. 13 (2023) 22852, https://doi.org/10.1038/s41598-023-49898-1.
[17] V.O. Sokolov, V.G. Plotnichenko, E.M. Dianov, The origin of near-IR luminescence in bismuth-doped silica and germania glasses free of other dopants: First-principle study, Opt. Mat. Express 3 (8) (2013) 1059–1074, https://doi.org/10.1364/OME.3.001059.
[18] S.V. Firstov, S.V. Alyshev, K.E. Riumkin, A.M. Khegai, A.V. Kharakhordin, M. A. Melkumov, E.M. Dianov, Laser-active fibers doped with bismuth for a wavelength region of 1.6–1.8 μm, IEEE J. Sel. Top. Quantum Electron. 24 (5) (2018) 0902415, https://doi.org/10.1109/JSTQE.2018.2801461.
[19] Z. Zhai, A. Halder, J.K. Sahu, High gain bismuth-doped fiber amplifier operating in the E+S band with record gain per unit length, J. Light. Technol. 42 (15) (2024) 5375–5382, https://doi.org/10.1109/JLT.2024.3417823.
[20] F.A. Cotton, Chemical Applications of Group Theory, third ed., John Wiley & Sons Inc., 1990. ISBN 0-471-51094-7.
[21] R.S. Drago, Physical Methods for Chemists, second ed., Surfside Scientific Publishers, 1992. ISBN 0-03-075176-4.
[22] D.C. Harris, M.D. Bertolucci, Symmetry and Spectroscopy : an Introduction to Vibrational and Electronics Spectroscopy, Dover Publications, Inc., 1989. ISBN 0-486-66144-X.
[23] E.V. Condon, G.H. Shortley, The Theory of Atomic Spectra, Cambridge University Press, 1953. ISBN 978-0-521-09209-8.
[24] S. Yoo, C. Basu, A.J. Boyland, C. Sones, J. Nilsson, J.K. Sahu, D. Payne, Photodarkening in Yb-doped aluminosilicate fibers induced by 488 nm irradiation, Opt. Lett. 32 (12) (2007) 1626–1628, https://doi.org/10.1364/OL.32.001626.